

Production of $\gamma Z g$ and associated processes via gluon fusion at hadron colliders

Pankaj Agrawal* and Ambresh Shrivastava†

Institute of Physics, Sainik School Post, Bhubaneswar 751 005, India

Abstract

We present results for the process $gg \rightarrow \gamma Z g$ within the standard model at hadron colliders. Due to large gluon flux at the LHC and the proposed HE-LHC, this process can have significant cross section at these machines. Several thousand such events have already been produced at the LHC according to the standard model predictions. This process can also be a background to new physics signals. We discuss some of the important features of this process related to the structure of its amplitude. We also compute the total cross section at the hadron colliders and give some important kinematic distributions. A comparison of our results is made with the corresponding NLO calculation using MCFM program. We briefly discuss the production of $\gamma\gamma g$ and $\gamma\gamma Z$ via gluon fusion. The amplitude of these processes are closely related to the $gg \rightarrow \gamma Z g$ amplitude.

1 Introduction

The quest for new physics signals is continuing at the Large Hadron Collider (LHC). The collider is presently running at 8 TeV center-of-mass energy and more than 10 fb^{-1} of data has been collected so far. The standard model (SM) is in excellent agreement with the collected data [1]. The recent discovery of a fundamental boson in the mass range of 125-126 GeV might confirm the existence of the long sought Higgs boson of the SM [2]. With the LHC running in the multi-TeV range, the gluon-gluon scattering processes that at the leading-order proceed via quark-loop diagrams can be important. Observation of such processes can be a significant test of the SM predictions. Many of such processes have been computed in the past. Processes with two or more electro-weak vector bosons in the final state have been studied extensively in the literature [3, 4, 5, 6, 7, 8, 9, 10, 11, 13, 14, 15]. In this paper, we study the $\gamma Z g$ production via gluon fusion in detail. The process $gg \rightarrow \gamma Z g$ contributes to the cross section of the process $pp \rightarrow \gamma Z j + X$ at the NNLO in α_s . The amplitude of this process, which occurs at the one-loop level, is finite and gauge invariant. Partial results for this process were reported in [11, 15]. We found that its contribution at the LHC, compared to the corresponding tree-level contribution, was about 4-5 % for a given set of kinematic cuts applied on the final state particles. This percentage would increase at higher center-of mass energy machines such as HE-LHC. In this detailed study, we check the decoupling of the top quark at the amplitude-squared and the total cross section level. We quantify the contribution of vector and axial-vector parts of the $\gamma Z g$ amplitude towards the total cross section. We also study the scale dependence and the effect of choosing specific parton distribution set. In addition, we consider the processes $gg \rightarrow \gamma\gamma g$ and $gg \rightarrow \gamma\gamma Z$ and briefly

*email:agrawal@iopb.res.in

†email:ambresh@iopb.res.in

discuss the results at the LHC. The process $gg \rightarrow \gamma\gamma g$ at the LHC has already been discussed in [10, 11]. We include the heavy top-quark in the loop to see if it decouples at the current energies. The NLO QCD corrections to the hadronic processes, $pp \rightarrow \gamma Z j + X$ and $pp \rightarrow \gamma\gamma Z + X$ are presented in [16, 17]. In the next section, we discuss the structure of the full amplitude. The method of calculation and numerical checks are presented in the section 3. In the section 4, we present our numerical results. We conclude in the last section.

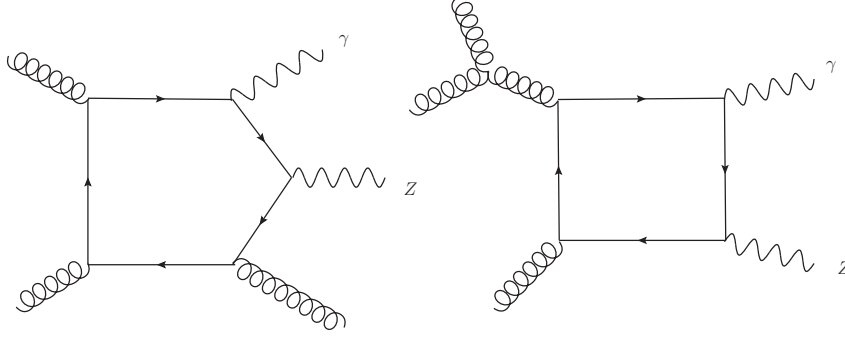


Figure 1: The prototype diagrams for the processes $gg \rightarrow g\gamma Z$.

2 The Amplitude

This one-loop process $gg \rightarrow \gamma Z g$ receives contribution from two main classes of quark-loop diagrams —pentagon and box type, as shown in Fig. (1). Box class of diagrams are due to the triple gluon vertices and can be further divided into three sub-classes. This sub-classification has its own physical importance as we will see later. Other diagrams can be obtained by suitable permutation of external legs. For each quark flavor, there are 24 pentagon-type and $3 \times 6 (= 18)$ box-type diagrams. However, only half of the 42 diagrams are independent. Using Furry's theorem, we can see that axial-vector contributions of the box diagrams add up to zero. Therefore, the box diagrams give only vector contribution. Pentagon diagrams give both vector and axial-vector contributions. We work with all six quark flavors. Except top-quark, we treat all other quarks as massless. The amplitude for our process has very nice structure. This is explained in detail in [12]. The full amplitude, after including contributions from all six quark flavors, has following form

$$\mathcal{M}^{abc}(gg \rightarrow \gamma Z g) = i \frac{f^{abc}}{2} \mathcal{M}_V + \frac{d^{abc}}{2} \mathcal{M}_A, \quad (1)$$

$$\begin{aligned} \mathcal{M}_V = \mathcal{A}_P^V - \mathcal{A}_B^V &= -\frac{e^2 g_s^3}{\sin\theta_w \cos\theta_w} \left[\left(\frac{7}{12} - \frac{11}{9} \sin^2\theta_w \right) \mathcal{M}_V^{(0)} \right. \\ &\quad \left. + \left(\frac{1}{6} - \frac{4}{9} \sin^2\theta_w \right) \mathcal{M}_V^{(t)} \right], \end{aligned} \quad (2)$$

$$\mathcal{M}_A = \mathcal{A}_P^A = \frac{e^2 g_s^3}{\sin\theta_w \cos\theta_w} \left[\frac{7}{12} \mathcal{M}_A^{(0)} + \frac{1}{6} \mathcal{M}_A^{(t)} \right]. \quad (3)$$

$\mathcal{M}_{V,A}$ are color ordered amplitudes for the vector and axial-vector parts of the amplitude. \mathcal{A}_B^V and $\mathcal{A}_P^{V,A}$ include full box and pentagon contributions for all six quark flavors. $\mathcal{M}_{V,A}^{(0)}$ and $\mathcal{M}_{V,A}^{(t)}$ represent light

quark and t -quark contributions respectively. It is clear from the structure of the amplitude that the vector and axial-vector contributions are separately gauge invariant. Therefore, the cross section of the process is an incoherent sum of the vector and axial-vector contributions.

The process $gg \rightarrow \gamma\gamma g$ proceeds via pentagon and box type of quark-loop diagrams and the amplitude is purely vector type. On the other hand the process $gg \rightarrow \gamma\gamma Z$ proceed via pentagon type quark loop diagrams only and its amplitude is purely axial-vector type. The structure of full amplitudes for these processes are

$$\mathcal{M}^{abc}(gg \rightarrow \gamma\gamma g) = i \frac{f^{abc}}{2} \mathcal{M}_V, \quad (4)$$

$$\mathcal{M}_V = \mathcal{A}_P^V - \mathcal{A}_B^V = -e^2 g_s^3 \left[\left(\frac{11}{9} \right) \mathcal{M}_V^{(0)} + \left(\frac{4}{9} \right) \mathcal{M}_V^{(t)} \right]. \quad (5)$$

$$\mathcal{M}^{ab}(gg \rightarrow \gamma\gamma Z) = \frac{\delta^{ab}}{2} \mathcal{M}_A, \quad (6)$$

$$\mathcal{M}_A = \mathcal{A}_P^A = \frac{e^3 g_s^2}{\sin\theta_w \cos\theta_w} \left[\left(\frac{5}{36} \right) \mathcal{M}_A^{(0)} + \left(\frac{1}{9} \right) \mathcal{M}_A^{(t)} \right]. \quad (7)$$

Our goal is now to compute \mathcal{M}_V and \mathcal{M}_A for the light quarks and the top-quark loops. The procedure is outlined in the next section.

3 Calculation and Numerical Checks

It would be sufficient to focus on the calculation of $gg \rightarrow \gamma Z g$ amplitude; other two processes can be considered as special cases of this process with appropriate changes in color and coupling factors. Our calculation is based on the traditional Feynman diagram method. We write down the prototype amplitudes for each class of diagrams using the SM Feynman rules. The amplitude of all other diagrams are generated by appropriately permuting the external momenta and polarizations in our code. Only one prototype pentagon amplitude is sufficient if we keep Z -boson external leg fixed in all permutations.¹ The quark-loop traces are calculated using FORM [18] in n -dimensions for the vector contributions. For the axial-vector contribution, the quark-loop trace is calculated in 4-dimensions. Interestingly, it turns out that the amplitude for the top-quark in the loop and a massless quark in the loop can be written in such a way that they have same analytical form in terms of tensor integrals. The dependence on the top-quark mass enters only through the reduction of tensor integrals. This is of considerable importance because it reduces the length and evaluation time of the amplitude with the top-quark in the loop. In the case of pentagon-type diagrams, the most complicated integral is rank-5 tensor integral ($E^{\mu\nu\rho\sigma\delta}$); while for the box-type diagrams, rank-4 tensor integral ($D^{\mu\nu\rho\sigma}$) is the most complicated one. Five point tensor and scalar integrals are written in terms of box tensor and scalar integrals using 4-dimensional Schouten Identity. The box tensor integrals are reduced into the standard scalar integrals – A_0 , B_0 , C_0 and D_0 that follow from the reduction scheme developed by Oldenborgh and Vermaseren [19]. These reduction procedures were implemented using Mathematica. We then obtain FORTRAN routines that compute various tensor integrals in terms of lower-rank tensor integrals and scalar integrals. The required scalar integrals are calculated using OneLoop library [21]. Because of very large and complicated expression of the amplitude, we calculate the amplitude numerically before squaring it. This requires numerical evaluation of the polarization

¹This is particularly economical when considering axial vector contributions for massive quark case.

vectors of gauge bosons. We choose real basis, instead of helicity basis for the polarization vectors to calculate the amplitude. This is to reduce the size of compiled program and the time taken in running the code. The three-body phase space is generated using RAMBO [22].

The amplitude for $gg \rightarrow \gamma Zg$ is a one-loop amplitude at the leading order (LO) itself. Though individual diagrams may be UV and/or IR divergent, the full amplitude should be both UV as well as IR finite. IR divergence is relevant to massless quark cases only. All these singularities are encoded in various scalar integrals. To make UV and IR finiteness check on our amplitude we have derived all the required scalar integrals analytically following t'Hooft and Veltman [23]. We regulate the UV divergence of the scalar integrals using dimensional regularization and infrared singularities by giving small mass to the quark, the mass regularization. Following are the details of various checks made on our amplitude.

1. *UV Finiteness:*

The tadpole and bubble scalar integrals (A_0 and B_0) are sources of UV singularity in any one loop amplitude. For the case of massless internal lines, A_0 s don't appear in the tensor reduction. For both the massive and massless quark contributions, we have verified that the amplitude is UV finite. The amplitude of each pentagon diagram has only UV finite tensor integrals. Therefore, each pentagon diagram is UV finite by itself as expected from naive power counting. The box diagrams individually are not UV finite. Therefore, the cancellation of the divergence in the sum of the box diagrams results is an important check. We find that the three classes of box diagrams are separately UV finite.

2. *IR Finiteness:*

The diagrams with massless internal quarks have mass singularities. Even with small quark mass (like bottom quark) these diagrams may have large logarithms which should cancel for the finiteness of the amplitude. There can be $\log^2(m_q^2)$ and $\log(m_q^2)$ types of singular terms. We have checked explicitly that such terms are absent from the amplitude. We have verified that the IR finiteness holds for the three classes of box amplitudes and pentagon amplitude separately.

3. *Ward Identities:*

Certain mathematical identities can be obtained by replacing a polarization vector by its 4-momentum in any of the pentagon/box amplitudes. This way a pentagon amplitude can be written as a difference of two (reduced) box amplitudes and also a box amplitude can be written as a difference of two (reduced) triangle amplitudes. In the appendix, we have written these identities for a prototype pentagon and a prototype box amplitude. We have verified them numerically. These Ward-Identities are important checks on individual diagrams and can also be utilized for a systematic study of numerical instabilities in tensor reduction near exceptional phase space points.

4. *Gauge Invariance:*

As we have seen, because of the color structure, the vector and axial-vector part of the amplitudes do not interfere and are separately gauge invariant. The vector part of the amplitude has gauge invariance with respect to three gluons, the photon and the Z -boson. This has been checked by replacing the polarization vector of any of these gauge particles by its momentum ($\varepsilon^\mu(p_i) \rightarrow p_i^\mu$) which makes the amplitude vanish. As one would expect the pentagon and three classes of box contributions are separately gauge invariant with respect to the γ and Z -boson. For each gluon,

one of the three classes of box amplitudes is separately gauge invariant and further cancellation takes place among pentagon and the other two box contributions. The axial-vector part of the amplitude is separately gauge invariant with respect to the all the three gluons and the photon. We verify that due to explicit breaking of the chiral symmetry in the presence of quark mass, the axial part of the amplitude vanishes on replacing Z -boson polarization by its 4-momentum only in the $m_q \rightarrow 0$ limit.

5. *Decoupling of heavy quarks:*

As a consistency check we have also verified that the vector and axial-vector parts of the amplitude vanish in the large quark mass limit [25]. This feature of the amplitude is very closely related to its UV structure. The decoupling holds for each pentagon amplitude and also for each class of box amplitudes.

Apart from making all above checks we have confirmed that the vector part of the $\gamma Z g$ amplitude (ignoring coupling factors) reproduces the $\gamma\gamma g$ amplitude in the $M_Z \rightarrow 0$ limit within the working precision.

4 Numerical Results

Based on the procedure outlined above, we can now compute the cross section and examine various features of the processes. As we have already mentioned, we compute amplitudes numerically using real polarization vectors for gauge bosons. For the processes $gg \rightarrow \gamma Z g$ and $gg \rightarrow \gamma\gamma Z$, there are total 48 polarized amplitudes to be computed for each phase space point; while for the $gg \rightarrow \gamma\gamma g$ process, there are 32 such amplitudes. Given the number of diagrams, the number of polarization combination and the length of the amplitude, the computation becomes very time consuming. Each phase space point evaluation takes about 1.3 seconds on a single machine that we use. We, therefore, run the code in parallel environment using AMCI package, a PVM implementation of the VEGAS algorithm [27, 28]. We have used more than 30 cores to run the code in parallel environment. Still it takes more than 12 hours to get suitable cross section which includes both massive and massless quark contributions. We use ifort compiler on Intel Xeon CPU 3.20GHz machines.

We first study the importance of the diagrams with the top-quark in the loop. For the process $gg \rightarrow \gamma Z g$, in Fig. (2), we plot the ratio of amplitude-squared for five and six quark flavor contributions as a function of the top-quark mass for a given phase space point. The partonic center-of-mass energy, \sqrt{s} is fixed at $8M_Z$. Vector and axial-vector contributions are plotted separately. The $m_t = 4M_Z$ corresponds to the scale above which the top-quarks in the loop can not go on-shell. Various slope changes shown in this plot correspond to possibilities of producing one or more final state particles via on-shell $t\bar{t}$ annihilation. In Fig. (3), we see that the contribution of the top-quark ($m_t = 175$ GeV) to the total cross section is negligible. We also see a knee in the plot at $m_t = \frac{M_Z}{2}$. This corresponds to the Z -boson production with $t\bar{t}$ annihilation. The top-quark decouples at around 100 GeV. We have, therefore, not included its contribution in our results presented below. The run time of our code is also reduced by 50%. It is not surprising that the top-quark decouples at such a low value for our processes. This is simply because there are four/five quark propagators in each box/pentagon diagram leading to a large power of the top-quark mass in the denominator.

We can divide our numerical results that are presented in this paper into two categories. We first discuss theoretical results, related to the structure of the amplitude, keeping Z -boson on-shell. Theoretical results presented below include following kinematic cuts: $p_T^j > 30$ GeV, $p_T^{\gamma, Z} >$

20 GeV, $|\eta^{\gamma,Z,j}| < 2.5$, $R(\gamma, j) > 0.6$. These cuts, together with $R(\gamma, \gamma) > 0.6$, are also used to compute total cross sections for $\gamma\gamma g$ and $\gamma\gamma Z$ cases. We have chosen factorization and renormalization scales as $\mu = \mu_F = \mu_R = E_T^Z$, the transverse energy of the Z -boson. Results are obtained using CTEQ6M parton distribution functions [29]. In Fig. (4), we present dependence of total cross section on collider centre-of-mass energy to see the effect of large gluon luminosity at higher energies. We have already seen that the vector and axial-vector parts of the amplitude are separately gauge invariant. Their contributions towards total cross section are also included in the figure. The axial-vector contribution is only about 10% of the total cross section; this contribution comes from the pentagon class of diagrams only. Although the box-contribution to the cross section is not separately gauge invariant with respect to the gluons, it is gauge invariant with respect to the γ and Z -boson. We find that more than 70% of the total cross section is due to the box-amplitude only, see Fig. (5). The scale variation of the total cross section about the central value $\mu = E_t^Z$ is shown in Fig. (6). On increasing the scale by a factor of 2, the cross section decreases by about 25%; it increases by about 40% on decreasing the scale by a factor of 2. These large variations are expected because our calculation is effectively LO as far as μ dependence is concerned. We see that the cross section falls as we increase the scale μ . This is because an increase in the factorization scale increases the cross section due to increase in gluon luminosity; but an increase in the renormalization scale decreases the cross section because of the decrease in the value of $\alpha_s(\mu)$. When we increase both the scales at the same time, the effect of the change in renormalization scale is stronger. It leads to an overall decrease in the cross section with the increase in the scale μ .

Next, we come to the discussion on our phenomenological results. These results include various kinematic distributions related to final state particles. For phenomenological results, we work in the narrow width approximation. We allow Z -boson to decay into two leptons in the phase space. In this case the kinematic cuts are,

$$p_T^j > 30 \text{ GeV}, p_T^\gamma > 15 \text{ GeV}, p_T^l > 10 \text{ GeV}, |\eta^{\gamma,l,j}| < 2.5, \\ R(\gamma, j), R(l, \gamma), R(l, j), R(l, l) > 0.4.$$

For convenience we have chosen the scale $\mu = \mu_F = \mu_R = M_Z$. In Fig. (7), we give cross section variation in the range of 8 to 14 TeV center-of-mass energy using both CTEQ6l1 and CTEQ6M parton distribution functions. These numbers do not include the branching ratio of $Z \rightarrow l^+l^-$. In particular, the cross sections, with CTEQ6l1 (CTEQ6M) parton distributions, are 65.4 (53.0) fb and 202.4 (154.3) fb at 8 TeV and 14 TeV center-of-mass energies respectively. With these cross sections, number of $gg \rightarrow \gamma Z g$ events can be as large as 20000 at 14 TeV LHC, with 100 fb^{-1} integrated luminosity. However, to observe these events, one may have to look at $Z \rightarrow l^+l^-$ decay channel; here l can be an electron/muon. So including the branching ratios, one may expect more than 1000 $gg \rightarrow \gamma Z(\rightarrow l^+l^-)g$ events. The transverse momentum and rapidity distributions for the final state particles are shown in Figs. (8-13) at 8 TeV center-of-mass energy. We have given normalized distributions as they remain same for different choices of parton distributions and/or scales. These distributions are characteristically similar at different collider center-of-mass energies but at higher energies contribution coming from high p_T /rapidity region grows while low p_T /rapidity region contribution goes down. We note that p_T^j is softer as compared to p_T^γ . It is because the cross section is dominated by the box class of diagrams and in these diagrams, the gluon is emitted as a bremsstrahlung radiation. Due to the same reason, *i.e.*, the gluon is emitted more collinearly, the rapidity distribution of the gluon is broader as compared to that of the photon. The lepton- p_T distribution peaks around $M_Z/2$. On the other hand the rapidity distribution of lepton is more central compared to the η^γ distribution.

\sqrt{S} (TeV)	$p_T^{\gamma,min}$ (GeV)	σ^{LO} (pb)	σ^{NLO} (pb)	σ_{gg}^{NNLO} (fb)	$\sigma^{NNLO}/\sigma^{NLO}(\%)$
8	30	2.202	2.560	46.05 (38.25)	1.8 (1.5)
	50	1.144	1.289	30.49 (25.61)	2.4 (2.0)
14	30	4.868	5.490	158.72 (124.48)	2.9 (2.3)
	50	2.608	2.803	109.92 (86.61)	3.9 (3.1)
35	30	14.973	17.069	854.09 (606.07)	5.0 (3.6)
	50	8.220	8.898	607.35 (438.88)	6.8 (4.9)

Table 1: Cross sections for the production of $pp \rightarrow \gamma Z j + X$ at various collider center-of-mass energies. We use CTEQ6l1 PDF set at LO and CTEQ6M PDF set at NLO. The NNLO predictions are with CTEQ6l1(CTEQ6M) parton distribution. The factorization and renormalization scales are set to $\mu_F = \mu_R = M_Z$.

We have also compared results of this NNLO calculation with the LO and NLO predictions for $pp \rightarrow \gamma(Z \rightarrow \nu\bar{\nu})j + X$ [16]. The LO and NLO results are obtained using parton-level next-to-leading order program MCFM². The comparison is presented after removing the branching ratios in Table 1. The table includes results at three different center-of-mass energies and for two values of the $p_T^{\gamma,min}$. We have included the center-of-mass energy of 35 TeV, as it is proposed for the HE-LHC collider. The other kinematic cuts are: $p_T^j > 30$ GeV, $p_T^{miss} > 30$ GeV, $|\eta^{\gamma,j}| < 2.5$, $R(\gamma, j) > 0.4$. This table illustrates two facts – 1) the fraction of NNLO events increases with the increase in $p_T^{\gamma,min}$, 2) the NNLO process becomes more important as we increase the center-of-mass energy. There is an increase in the NNLO fraction with an increase in $p_T^{\gamma,min}$ because, in the NLO events, photon is emitted from a quark line; so a larger $p_T^{\gamma,min}$ suppresses the NLO contribution more than the NNLO contribution. In figure (14) we have compared the normalized p_T^{γ} -distributions at NLO and NNLO, leading to the same conclusion. The importance of the NNLO process is more at higher center-of-mass energy simply because of the increase in the gluon-gluon luminosity.

The variation of the total cross section with collider centre-of-mass energy for $\gamma\gamma g$ and $\gamma\gamma Z$ production via gluon fusion are given in Figs. (15) and (16) respectively. We reconfirm the importance of $gg \rightarrow \gamma\gamma g$ at the LHC. Like the $gg \rightarrow \gamma Z g$ process, we have checked that the diagrams with the top-quark in the loop make negligible contribution. The cross section at the 14 TeV centre-of-mass energy is of the order of 2 pb, leading to several thousand events with even 1 fb^{-1} of integrated luminosity. The amplitude for $gg \rightarrow \gamma\gamma Z$ is purely axial-vector type and the coupling factors are smaller as compared to the axial-vector part of the $\gamma Z g$ amplitude. We find that its cross section is very small at the LHC, about 0.02 fb. Therefore, this process is unlikely to be observed at the LHC.

Like other calculations of our types, we have also faced the issue of numerical instability in our calculation for certain phase space points. This is a well known issue with the reduction of one-loop tensor integrals of higher rank and higher points. This issue is also faced in the evaluation of scalar integrals. We face numerical instabilities in the evaluation of pentagon-tensor integrals. This is related to the inaccurate evaluation of Gramm determinants in those phase space regions where the linear independency of external momenta (modulo 4-momentum conservation) is compromised. The inverse Gramm determinants appear in the reduction of tensor integrals. Near exceptional phase space points the Gramm determinants become very small and give rise to numerical problems because of loss of precision due to large cancellation. This problem can be handled in several ways. One way is to

²<http://mcfm.fnal.gov/>

use higher precision for tensor reduction and scalar integral calculations. This certainly reduces the number of exceptional phase space points but the code becomes enormously slow. Another approach could be to use special expressions for tensor reduction for such phase space points. This approach is some time better. It is important to mention here that none of these two approaches cure the problem of numerical instability completely [26]. A more economic and convenient way to proceed in this situation is to judiciously ignore the contributions from such phase space points. This one can do because we are not doing precision calculations and exceptional phase space points are very special and are unlikely to give a significant contribution to the total cross section. We perform a gauge-invariance (GI) test on full amplitude for each phase space point. In practice, we put a GI test cut of, $\delta = 10^{-6}$ on amplitude-squared. We ignore all those points which fail to pass this test. With this cut on δ and other kinematic cuts, the number of points ignored are below 2%. However, with higher p_T cut and/or less stringent cut on the δ , the number of such points can drop to a level of 0.01%. We sample about 0.4-0.5 million phase space points to obtain the numerical results. Given the volume of phase space, the number of exceptional phase space points is small and it is reasonable to assume that the cross section is not dominated by this region of phase space. We find that our result depends on this cut very weakly and remains quite stable over the range of $10^{-4} - 10^{-12}$ for the choice of cut. This also reflects that the exceptional phase space points are few and make small contribution. This can be seen in Fig. (17). We have also checked our results for cross section calculation by implementing a set of Ward identity tests and its sensitivity on δ like cut parameter. Though the total cross section is quite stable, various distributions (specially the rapidity distributions near the edges) are quite sensitive to variation in δ . Edges of distributions define the region where exceptional phase space points may lie. Therefore, inaccuracy of the distributions at the edges of the phase space is not surprising. We have seen that the exceptional phase space points may defy the Ward identity tests sometimes. This might be related to the form of these identities as shown in eqns. (8) and (9)³. One can make these δ -like cuts more stringent to get more reliable distributions. One can also identify exceptional phase space points at the level of Gramm determinants which may be more economical. Phase space points corresponding to large cancellation in Gramm determinants can be ignored without putting stringent cuts on δ and again leading to more reliable distributions. A method to implement this criterion is discussed in [26].

5 Conclusions

In this paper, we have presented the results of the cross section calculations for the processes $gg \rightarrow \gamma Zg$, $gg \rightarrow \gamma\gamma g$ and $gg \rightarrow \gamma\gamma Z$ at the hadron colliders. These processes occur at the one-loop level via pentagon and box diagrams. We have made a number of checks on our calculation. We have verified the finiteness of the amplitude and have checked its gauge invariance with respect to all the gauge particles. We have also checked the decoupling of the heavy quark and some of the Ward identities which are listed in the Appendix. For the γZg process, the axial-vector contribution does not interfere with the vector contribution and it is separately gauge invariant.

Results are obtained using the parallel running of the code. We have presented the cross sections and various kinematic distributions mainly for the $gg \rightarrow \gamma Zj$ process. We find that the top-quark contribution is negligible; and that the vector coupling contributions dominate over the axial vector couplings. The typical cross section for the process $gg \rightarrow \gamma Zg$ is of the order of 100 – 200 fb. A comparison with MCFM suggests the contribution of this process to the NLO cross-section of $pp \rightarrow \gamma Zj$ is about 3 – 4%. One may be able to enhance this percentage further by choosing an

³ The actual implementation of Ward identities, say for pentagon diagrams, is in the form of, $(1 - \frac{\mathcal{M}_P}{\mathcal{M}_B^1 - \mathcal{M}_B^2}) < \delta$.

appropriate set of kinematic cuts. The amplitude for $gg \rightarrow \gamma\gamma g$ is purely vector type and its typical cross section is about 2 pb. Both these processes should be observable at the LHC. However, the process $gg \rightarrow \gamma\gamma Z$ is more suppressed due to it being a purely axial-vector pentagon process and it is unlikely to be seen at the LHC.

Acknowledgment

We would like to thank people involved in maintaining the small cluster facility of forty cores at the institute computer centre. AS would like to acknowledge fruitful discussions with Francisco Campanario on the issue of numerical instability. He also wishes to thank John M. Campbell for providing help with MCFM program.

6 Appendix: Ward-Identity for Pentagon and Box Amplitudes

We wish to write down the Ward-Identity for prototype pentagon and box diagrams shown in Fig. (1). We choose replacing Z polarization vector by its 4-momentum to setup pentagon identities. We ignore all the irrelevant factors of color and coupling etc. and consider vector part of the amplitude. It can easily be extended for axial-vector part of the amplitude.

$$\begin{aligned} \mathcal{M}_P(p_1, p_2, p_3, p_4; \epsilon_1, \epsilon_2 = p_2, \epsilon_3, \epsilon_4, \epsilon_5) &\equiv tr \left(\not{\epsilon}_5 \frac{1}{\not{k}_{1234} - m_q} \not{\epsilon}_4 \frac{1}{\not{k}_{123} - m_q} \not{\epsilon}_3 \frac{1}{\not{k}_{12} - m_q} \not{p}_2 \frac{1}{\not{k}_1 - m_q} \not{\epsilon}_1 \frac{1}{\not{k} - m_q} \right) \\ &= tr \left(\not{\epsilon}_5 \frac{1}{\not{k}_{1234} - m_q} \not{\epsilon}_4 \frac{1}{\not{k}_{123} - m_q} \not{\epsilon}_3 \frac{1}{\not{k}_1 - m_q} \not{\epsilon}_1 \frac{1}{\not{k}} \right) - tr \left(\not{\epsilon}_5 \frac{1}{\not{k}_{1234} - m_q} \not{\epsilon}_4 \frac{1}{\not{k}_{123} - m_q} \not{\epsilon}_3 \frac{1}{\not{k}_{12} - m_q} \not{\epsilon}_1 \frac{1}{\not{k} - m_q} \right) \\ &\text{where we have used, } \not{p}_2 = (\not{k}_{12} - m_q) - (\not{k}_1 - m_q). \end{aligned}$$

$$\begin{aligned} \Rightarrow \mathcal{M}_P(p_1, p_2, p_3, p_4; \epsilon_1, \epsilon_2 = p_2, \epsilon_3, \epsilon_4, \epsilon_5) &= \mathcal{M}_B(p_1, p_2 + p_3, p_4; \epsilon_1, \epsilon_3, \epsilon_4, \epsilon_5) \\ &\quad - \mathcal{M}_B(p_1 + p_2, p_3, p_4; \epsilon_1, \epsilon_3, \epsilon_4, \epsilon_5). \end{aligned} \quad (8)$$

Similarly we can write for the prototype box amplitude,

$$\begin{aligned} \mathcal{M}_B(p_1, p_2, p_3; \epsilon_1, \epsilon_2 = p_2, \epsilon_3, \epsilon_{45}) &= \mathcal{M}_T(p_1, p_2 + p_3; \epsilon_1, \epsilon_3, \epsilon_{45}) \\ &\quad - \mathcal{M}_T(p_1 + p_2, p_3; \epsilon_1, \epsilon_3, \epsilon_{45}). \end{aligned} \quad (9)$$

Here, ϵ_{45} denotes the triple gluon vertex attached to the box/triangle diagram. These Ward-Identities are shown diagrammatically in Fig. (18).

References

- [1] Andy Parker, *SUSY Searches (ATLAS/CMS)*; Steven Worm, *Searches for Beyond the Standard Model* (talks given at ICHEP 2012, Melbourne, Australia)
- [2] G. Aad *et al.* [The ATLAS Collaboration], arXiv:1207.7214 [hep-ex]; S. Chatrchyan *et al.* [The CMS Collaboration], arXiv:1207.7235 [hep-ex].
- [3] J. J. van der Bij and E. W. N. Glover, Phys. Lett. B **206**, 701 (1988).

- [4] E. W. N. Glover and J. J. van der Bij, Nucl. Phys. B **321**, 561 (1989).
- [5] E. W. N. Glover and J. J. van der Bij, Phys. Lett. B **219**, 488 (1989).
- [6] T. Binoth, M. Ciccolini, N. Kauer and M. Kramer, JHEP **0503**, 065 (2005) [hep-ph/0503094].
- [7] T. Binoth, M. Ciccolini, N. Kauer and M. Kramer, JHEP **0612**, 046 (2006) [hep-ph/0611170].
- [8] J. M. Campbell, R. K. Ellis and C. Williams, JHEP **1107**, 018 (2011) [arXiv:1105.0020 [hep-ph]].
- [9] J. M. Campbell, R. K. Ellis and C. Williams, JHEP **1110**, 005 (2011) [arXiv:1107.5569 [hep-ph]].
- [10] D. de Florian and Z. Kunszt, Phys. Lett. B **460**, 184 (1999) [hep-ph/9905283].
- [11] P. Agrawal and G. Ladinsky, Phys. Rev. D **63**, 117504 (2001) [hep-ph/0011346].
- [12] P. Agrawal and A. Shivaji, arXiv:1201.0511 [hep-ph].
- [13] T. Melia, K. Melnikov, R. Rontsch, M. Schulze and G. Zanderighi, arXiv:1205.6987 [hep-ph].
- [14] N. Kauer and G. Passarino, arXiv:1206.4803 [hep-ph].
- [15] P. Agrawal and A. Shivaji, arXiv:1207.2927 [hep-ph].
- [16] J. M. Campbell, H. B. Hartanto and C. Williams, arXiv:1208.0566 [hep-ph].
- [17] G. Bozzi, F. Campanario, M. Rauch and D. Zeppenfeld, Phys. Rev. D **84**, 074028 (2011) [arXiv:1107.3149 [hep-ph]].
- [18] J. A. M. Vermaseren, math-ph/0010025.
- [19] G. J. van Oldenborgh and J. A. M. Vermaseren, Z. Phys. C **46** (1990) 425.
- [20] W. L. van Neerven and J. A. M. Vermaseren, Phys. Lett. B **137**, 241 (1984).
- [21] A. van Hameren, Comput. Phys. Commun. **182**, 2427 (2011) [arXiv:1007.4716 [hep-ph]].
- [22] R. Kleiss, W. J. Stirling and S. D. Ellis, Comput. Phys. Commun. **40**, 359 (1986).
- [23] G. 't Hooft and M. J. G. Veltman, Nucl. Phys. B **153**, 365 (1979).
- [24] G. Duplancic and B. Nizic, Eur. Phys. J. C **20**, 357 (2001) [hep-ph/0006249].
- [25] T. Appelquist and J. Carazzone, Phys. Rev. D **11**, 2856 (1975).
- [26] F. Campanario, JHEP **1110**, 070 (2011) [arXiv:1105.0920 [hep-ph]].
- [27] S. Veseli, Comput. Phys. Commun. **108**, 9 (1998).
- [28] Message Passing Interface Forum, Int. J. Supercomp. Apps. 8, **157** (1994)
- [29] P. M. Nadolsky, H. -L. Lai, Q. -H. Cao, J. Huston, J. Pumplin, D. Stump, W. -K. Tung and C. -P. Yuan, Phys. Rev. D **78**, 013004 (2008) [arXiv:0802.0007 [hep-ph]].

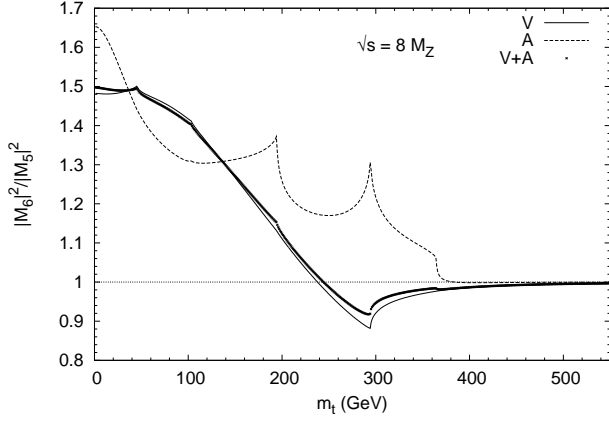


Figure 2: Decoupling of top quark. Vector and axial-vector contributions are shown separately.

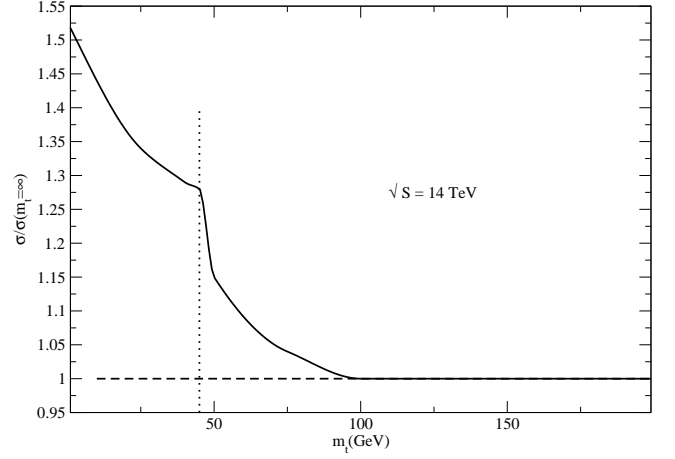


Figure 3: Decoupling of top quark in total cross section calculation for $gg \rightarrow \gamma Z g$.

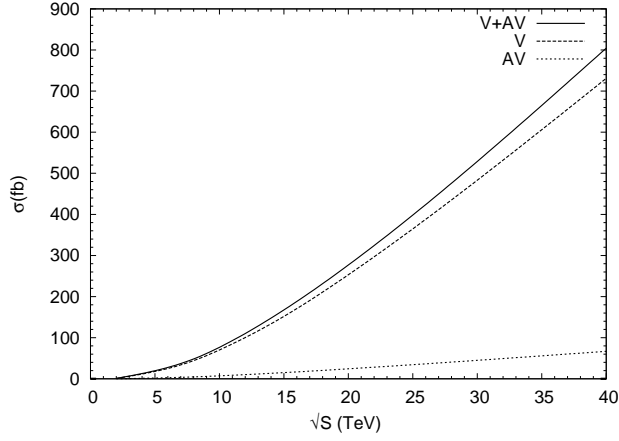


Figure 4: Vector and axial-vector contributions of total cross section.

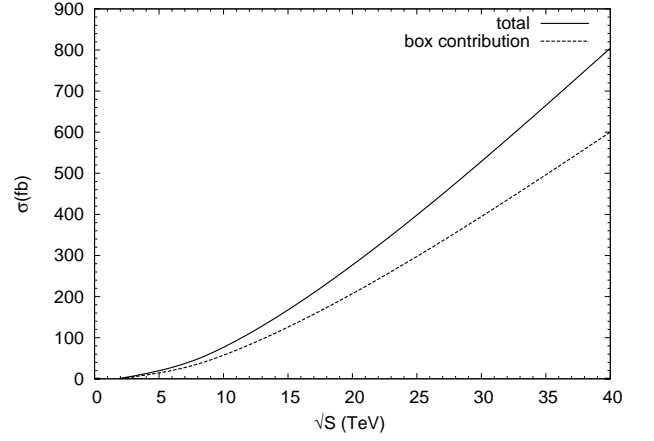


Figure 5: Contribution of box-amplitude towards the total cross section.

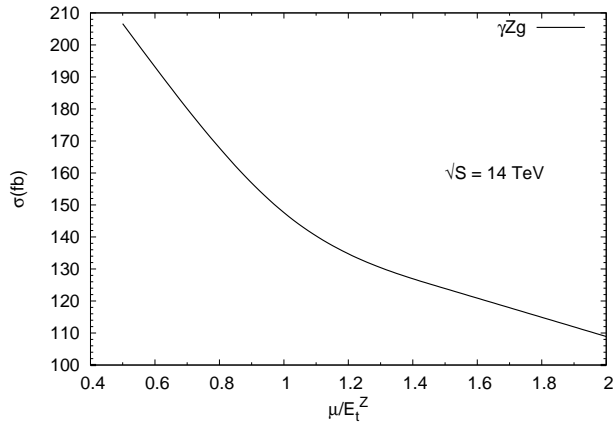


Figure 6: Variation of the total cross section with the scale, $\mu = \mu_R = \mu_F$.

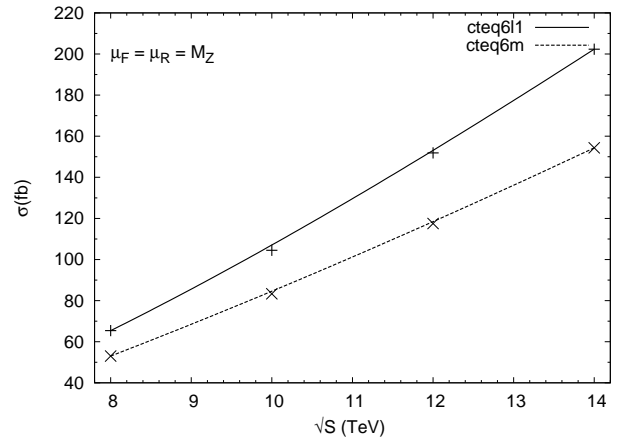


Figure 7: Dependence of total cross section on collider center-of-mass energy.

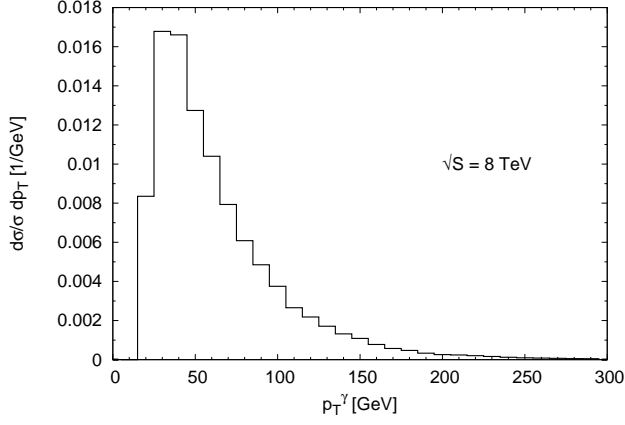


Figure 8: Transverse momentum distribution of γ at 8 TeV centre-of-mass energy.

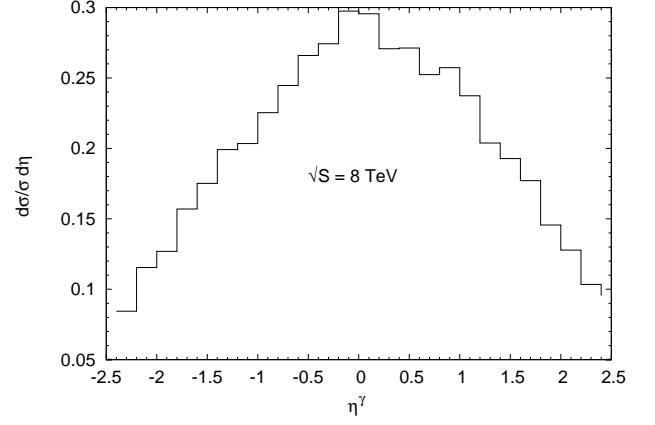


Figure 9: Rapidity distribution of γ at 8 TeV centre-of-mass energy.

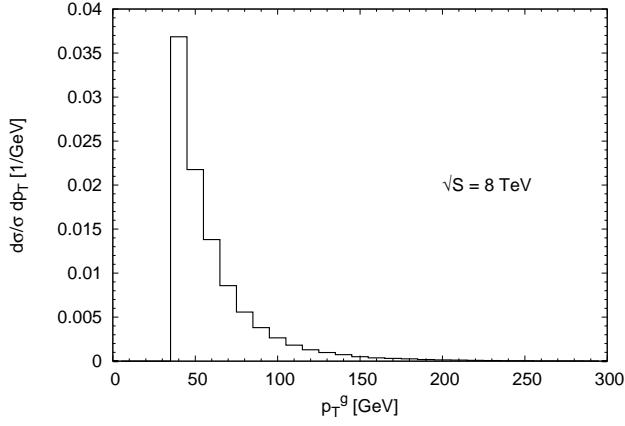


Figure 10: Transverse momentum distribution of g at 8 TeV centre-of-mass energy.

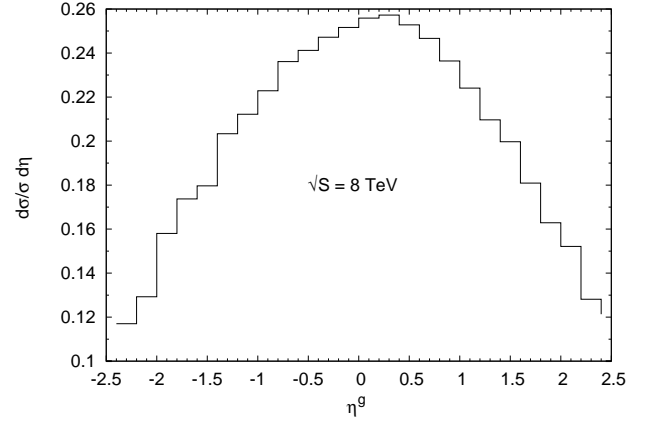


Figure 11: Rapidity distribution of g at 8 TeV centre-of-mass energy.

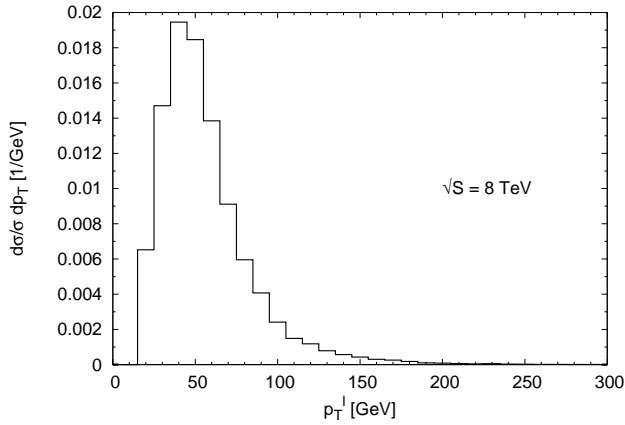


Figure 12: Transverse momentum distribution of lepton at 8 TeV centre-of-mass energy.

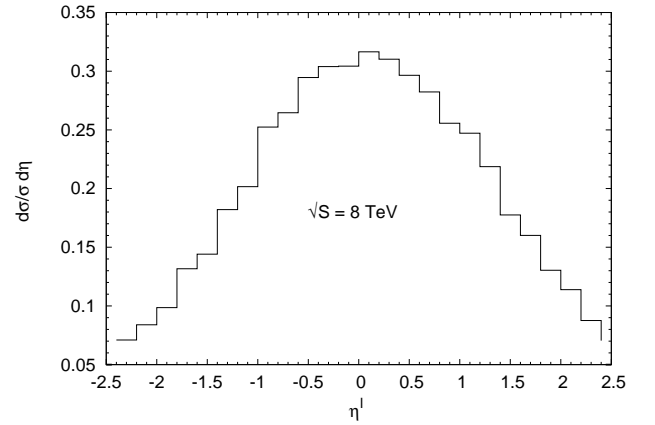


Figure 13: Rapidity distribution of lepton at 8 TeV centre-of-mass energy.

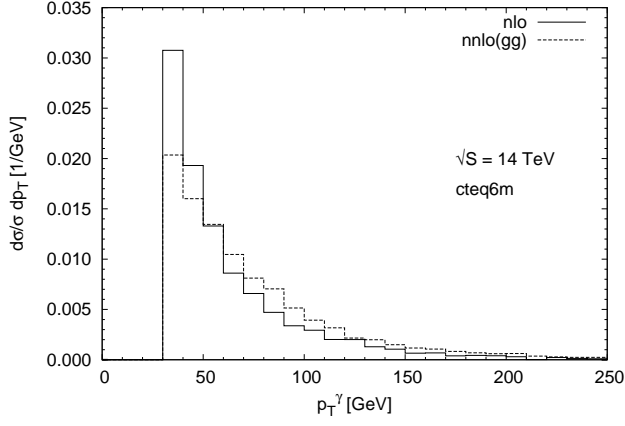


Figure 14: Comparison of normalized p_T distributions of γ at NLO and NNLO. NLO distribution is obtained using MCFM.

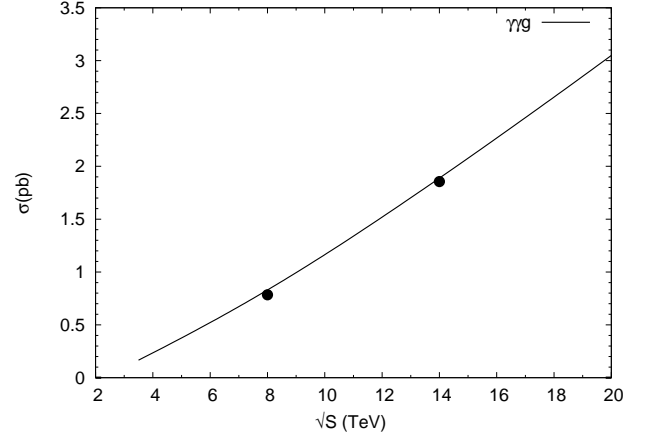


Figure 15: Variation of the total cross section with the centre-of-mass energy for $gg \rightarrow \gamma\gamma g$.

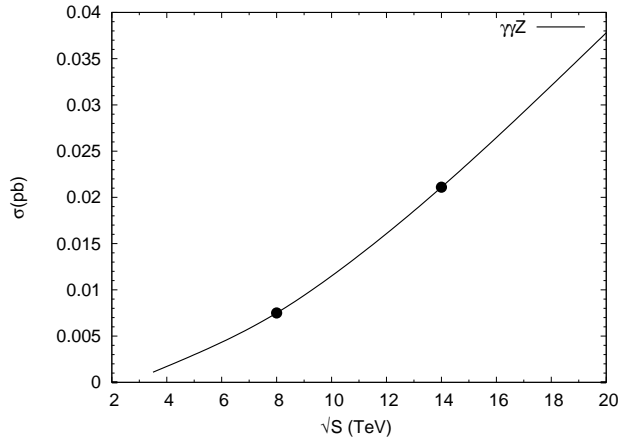


Figure 16: Variation of the total cross section with the centre-of-mass energy for $gg \rightarrow \gamma\gamma Z$.

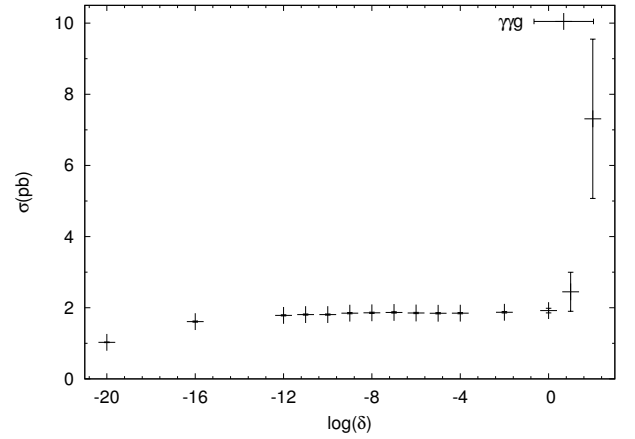


Figure 17: Dependence of total cross section for $\gamma\gamma g$ production on GI-test cut parameter, δ .

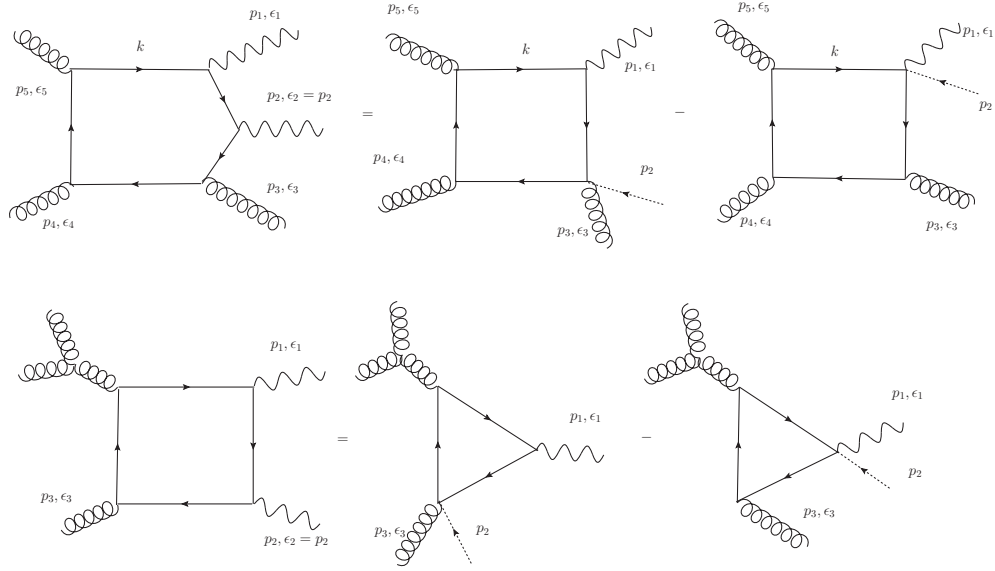


Figure 18: Ward-Identity for Pentagon and Box diagrams. All the momenta are taken incoming. The dotted lines take care of momentum insertion at relevant vertices.